PROCEEDINGS OF SCIENCE

Measurements of quartic coupling and vector boson scattering in ATLAS

Diana Pyatiizbyantseva[a,*] **on behalf of the ATLAS Collaboration**

[a] *Radboud University,*
Houtlaan 4, 6525 XZ Nijmegen, the Netherlands

E-mail: Diana.Pyatiizbyantseva@cern.ch

Measurements of multiboson production at the Large Hadron Collider (LHC) probe the electroweak gauge structure of the Standard Model for contributions from anomalous couplings. Vector boson scattering processes provide a unique opportunity to probe beyond the Standard Model physics via their sensitivity to quartic gauge boson couplings. This paper presents the recent ATLAS results on the measurement of electroweak production of a $Z\gamma$ pair in association with two jets when Z decays to neutrinos producing missing transverse energy.

Corfu Summer Institute 2022 "School and Workshops on Elementary Particle Physics and Gravity"
28 August - 1 October 2022
Corfu, Greece

*Speaker

PoS(CORFU2022)011

1. Introduction

$Z(\nu\bar{\nu})\gamma jj$ production is one of the processes to probe the nature of electroweak (EWK) symmetry breaking regulated by the Higgs boson in the Standard Model (SM). New phenomena could modify this regulation mechanism and cause measured values of quartic gauge couplings (QGCs) to differ from the SM predictions.

$Z\gamma jj$ final state is sensitive to the neutral QGCs which are absent in the SM at tree level but can be induced by beyond the SM (BSM) physics. Thus, the only allowed vertex for this vector boson scattering (VBS) process shown in Figure 1a is $WWZ\gamma$, while $ZZZ\gamma$, $ZZ\gamma\gamma$ and $Z\gamma\gamma\gamma$ couplings are forbidden. $Z\gamma jj$ QCD process (Figures 1b and 1c) with the same final state, but different interaction is the main background for the signal process.

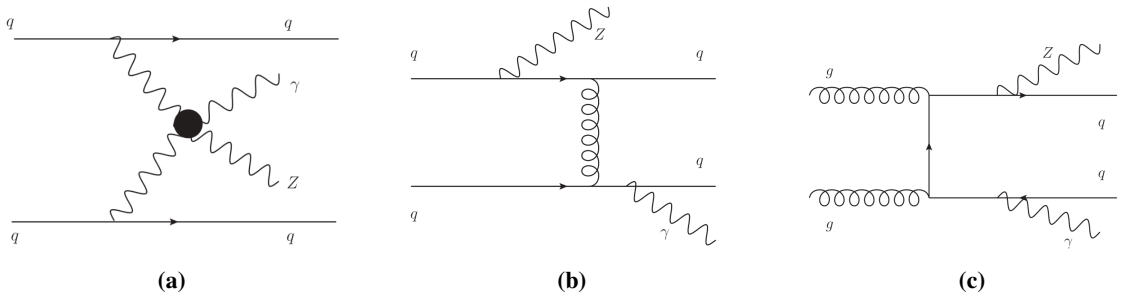

Figure 1: Feynman diagrams of EWK $Z\gamma jj$ production involving VBS processes (left) and $Z\gamma jj$ QCD production with gluon exchange (middle) and s-channel gg–qq process (right) [1].

The choice of the neutrino channel of Z boson decay is motivated by its higher branching ratio compared to the charged lepton one and better background control than in the hadronic decay channel.

The analysis [1] uses Run 2 data collected during 2015-2018 by the ATLAS experiment [2] from pp collisions at the centre-of-mass energy $\sqrt{s}$ = 13 TeV which corresponds to an integrated luminosity of 139 fb^{-1}.

2. Region definitions

A high-energy phase-space region called the $Z\gamma$ inclusive region is defined, as it is more sensitive to anomalous QGCs (aQGCs). It consists of at least two jets, one isolated photon with transverse energy $E_{\mathrm{T}}^{\gamma} > 150$ GeV, and missing transverse energy $E_{\mathrm{T}}^{\mathrm{miss}} > 120$ GeV corresponding to neutrino in the ATLAS experiment. A lepton veto is applied as no electrons and muons are expected in the final state. Events must satisfy the restriction on the calorimeter-measured $E_{\mathrm{T}}^{\mathrm{miss}}$ significance to be greater than 12. It is calculated as $|\vec{p}_{\mathrm{T}}^{\,\mathrm{miss}}|^2/\left(\sigma_{\mathrm{L}}^2\left(1-\rho_{\mathrm{LT}}^2\right)\right)$, where $\vec{p}_{\mathrm{T}}^{\,\mathrm{miss}}$ is the missing transverse momentum, σ_{L} is the total variance longitudinal to it, ρ_{LT} is the correlation coefficient of the longitudinal (L) and transverse (T) measurements [3]. Azimuthal angle separations between a photon and $\vec{p}_{\mathrm{T}}^{\,\mathrm{miss}}$ $|\Delta\phi(\gamma, \vec{p}_{\mathrm{T}}^{\,\mathrm{miss}})| > 0.4$, the leading jet j_1 with the highest p_{T} and $\vec{p}_{\mathrm{T}}^{\,\mathrm{miss}}$ $|\Delta\phi(j_1, \vec{p}_{\mathrm{T}}^{\,\mathrm{miss}})| > 0.3$, and the subleading jet j_2 with the second-highest p_{T} and $\vec{p}_{\mathrm{T}}^{\,\mathrm{miss}}$ $|\Delta\phi(j_2, \vec{p}_{\mathrm{T}}^{\,\mathrm{miss}})| > 0.3$ are used to suppress numerous background processes mentioned in Section 3.

The requirement on the *'soft term'* [4] of $\vec{p}_{\mathrm{T}}^{\,\mathrm{miss}}$, reconstructed with tracks from the primary vertex not associated with any physic objects, to be less than 16 GeV is also applied.

There are the signal region (SR) and several control regions (CRs) for the estimation of the backgrounds and checks for possible mismodelling (Figure 2). $W\gamma$ CR is used for the $W(\ell\nu)\gamma jj$ and $t\bar{t}\gamma jj$ background processes and it has the same definition as the $Z\gamma$ inclusive region but with requirements of at least one lepton. The selections for the SR are dijet invariant mass $m_{jj} > 300$ GeV and photon centrality < 0.6 $\left(\gamma\text{-centrality} = \left|\frac{y(\gamma)-0.5[y(j_1)+y(j_2)]}{y(j_1)-y(j_2)}\right|\right)$. For the $Z(\nu\bar{\nu})\gamma jj$ quantum chromodynamics (QCD) background estimation, the $Z\gamma$ QCD CR 1 with $m_{jj} < 300$ GeV is used. Possible m_{jj} mismodelling is checked using $Z\gamma$ QCD CR 2 with $m_{jj} > 300$ GeV and γ-centrality > 0.6.

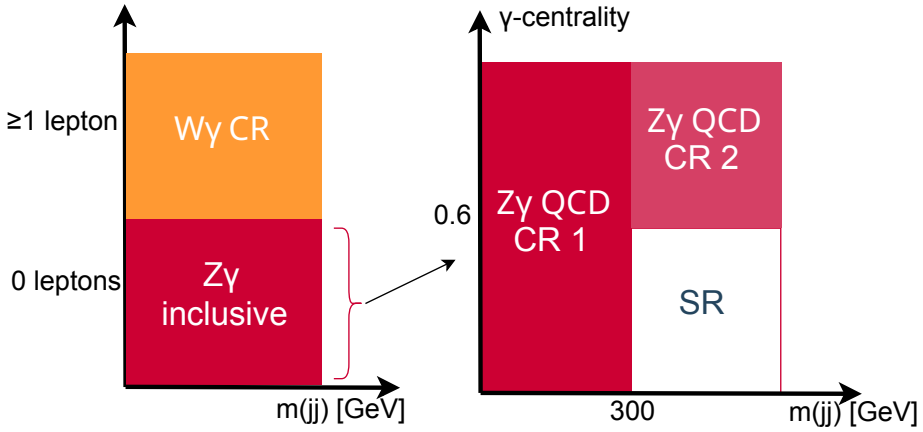

Figure 2: Definition of the regions used in the analysis [1].

3. Background composition

The greatest contribution to backgrounds comes from the $Z(\nu\bar{\nu})\gamma jj$ QCD process. It is estimated via simultaneous SR+CRs fit to data (with the shape from the Monte Carlo, MC, simulation) with $W(\ell\nu)\gamma jj$ and $t\bar{t}\gamma jj$ (semileptonic or fully leptonic decays) processes. The leptons are either not reconstructed ones or hadronic decaying τ-leptons.

There are several processes with object misidentification which are estimated from data. In electron to photon ($e \to \gamma$) misidentification ($W(e\bar{\nu})\gamma jj$, tjj, $t\bar{t}jj$ processes), W boson decays leptonically, but lepton's track is not reconstructed, and the final state electron is misidentified as a photon. This background is estimated using the 'tag&probe' method [5], where a lepton in $e^{\pm}\gamma$ pair with invariant mass near the Z boson mass is misidentified as a photon.

The source of the $j \to E_{\mathrm{T}}^{\mathrm{miss}}$ background (γjj) is an incorrect measurement of the jet energy or unreconstructed jets. To estimate this background, a two-dimensional sideband method [6] based on the $E_{\mathrm{T}}^{\mathrm{miss}}$ significance and $p_{\mathrm{T}}^{\mathrm{SoftTerm}}$ is used. The discriminating variables are chosen to build four orthogonal regions with inverted selections to decrease the correlation between them.

In $j \to \gamma$ background (Zj, jj) hadronic jets, in which the neutral mesons carry a significant fraction of the energy, may be misidentified as isolated photons due to similar calorimeter responses

(energy deposits). It is also estimated using the two-dimensional sideband method but based on photon isolation and identification.

Background from pile-up arises from a photon and Z boson produced in different pp collisions in the same bunch crossing. The pile-up background estimation is based on the longitudinal coordinate difference between the reconstructed primary vertex and the photon origin. The impact of this background is negligible.

$Z(\ell\bar{\ell})\gamma jj$ background is estimated via MC predictions.

4. Maximum-likelihood fit

For extracting the signal from the background processes a maximum-likelihood fit [7] is used. The Boosted Decision Tree (BDT) [8] classifier trained in the $Z\gamma$ inclusive region is created with the TMVA [9] package for $Z(\nu\bar{\nu})\gamma jj$, $W(\ell\nu)\gamma jj$ and $t\bar{t}\gamma jj$ processes. The list of variables used for creating the classifier contains: m_{jj}, $\Delta y(j_1, j_2)$, $E_{\mathrm{T}}^{\mathrm{miss}}$, p_{T}-balance $= \frac{|\vec{p}_{\mathrm{T}}^{\,miss}+\vec{p}_{\mathrm{T}}^{\,\gamma}+\vec{p}_{\mathrm{T}}^{\,j_1}+\vec{p}_{\mathrm{T}}^{\,j_2}|}{E_{\mathrm{T}}^{\mathrm{miss}}+E_{\mathrm{T}}^{\gamma}+p_{\mathrm{T}}^{j_1}+p_{\mathrm{T}}^{j_2}}$, $\eta(j_2)$, $p_{\mathrm{T}}(j_1)$, $\eta(\gamma)$, p_{T}-balance (reduced) $= \frac{|\vec{p}_{\mathrm{T}}^{\,\gamma}+\vec{p}_{\mathrm{T}}^{\,j_1}+\vec{p}_{\mathrm{T}}^{\,j_2}|}{E_{\mathrm{T}}^{\gamma}+p_{\mathrm{T}}^{j_1}+p_{\mathrm{T}}^{j_2}}$, N_{jets}, $\sin(|\Delta\varphi(j_1, j_2)/2|)$ and $\Delta y(j_1, \gamma)$. The fit uses the BDT response distribution in the SR and the m_{jj} distributions in the $Z\gamma$ QCD and $W\gamma$ CRs.

The signal strength parameter ($\mu_{Z\gamma\mathrm{EWK}}$) and the normalisation factors for $Z(\nu\bar{\nu})\gamma jj$ QCD background ($\mu_{Z\gamma\mathrm{QCD}}$) and $W(\ell\nu)\gamma jj$, $t\bar{t}\gamma jj$ processes ($\mu_{W\gamma}$) are free parameters in the fit. The systematic uncertainties are included in the likelihood function as the nuisance parameters (NPs) with Gaussian constraints. More detailed information about the systematic uncertainties is described in Section 6.

A background-only fit with $\mu_{Z\gamma\mathrm{EWK}} = 0$ is used to estimate the observed significance, while the expected significance is estimated using the fit to the Asimov data [10] in the same way. Figure 3 shows the BDT response distribution in the SR and the m_{jj} distributions in the $Z\gamma$ QCD and $W\gamma$ CRs after the fit with the summary plot on Figure 4.

Table 1 presents the event yields which are estimated in the fit to the observed data in the SR and CRs as well as the signal strength and background normalisation coefficients (the second column of Table 2).

The previous ATLAS measurement of the $Z(\nu\bar{\nu})\gamma jj$ EWK process [11] is done in the phase-space with $15 < E_{\mathrm{T}}^{\gamma} < 110$ GeV which is orthogonal in this variable to the current analysis. The result of this analysis is shown in the third column of Table 2, while the combination with the current analysis is in the last column of Table 2 which increases the sensitivity.

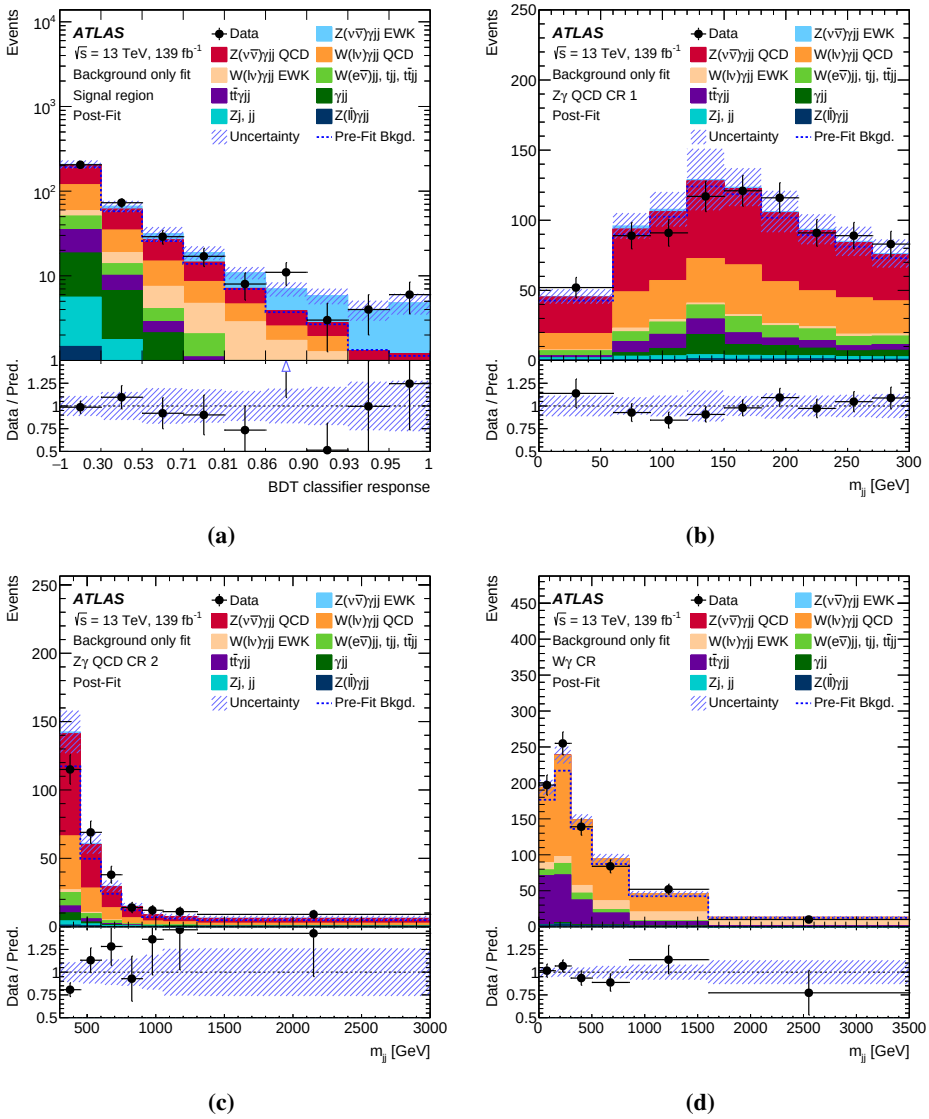

Figure 3: The BDT response distribution in the SR and the m_{jj} distributions in the $Z\gamma$ QCD and $W\gamma$ CRs after the fit with the ratio of the observed to expected results [1].

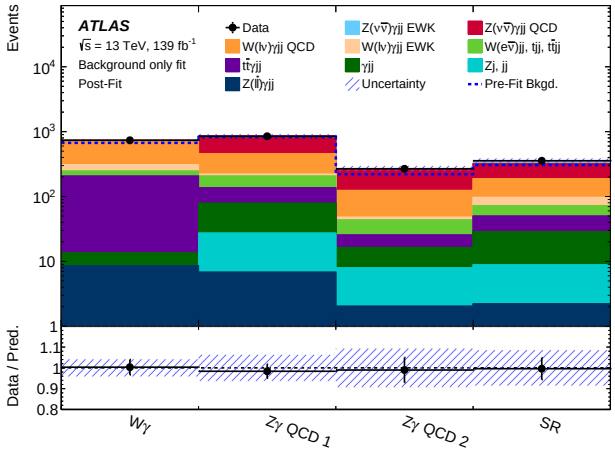

Figure 4: Summary plot of the event yields after the fit in all regions with the ratio of the observed to expected results [1].

Table 1: Observed and expected event yields with the combination of statistical and systematic uncertainties for the signal and background processes after the fit [1].

	$W\gamma$ CR	$Z\gamma$ QCD CR 1	$Z\gamma$ QCD CR 2	Signal region
$Z(\nu\bar{\nu})\gamma jj$ EWK	0.108 ± 0.028	11.0 ± 4.3	4.0 ± 2.2	37 ± 14
$Z(\nu\bar{\nu})\gamma jj$ QCD	1.04 ± 0.46	394 ± 84	143 ± 32	133 ± 39
$W(\ell\nu)\gamma jj$ QCD	425 ± 63	237 ± 71	76 ± 24	91 ± 30
$W(\ell\nu)\gamma jj$ EWK	63 ± 12	14.3 ± 2.7	4.5 ± 1.2	24.6 ± 4.9
$W(e\nu)jj, tjj, t\bar{t}jj$	39.8 ± 2.5	70.1 ± 4.1	17.9 ± 1.3	22.5 ± 1.5
$t\bar{t}\gamma jj$	193 ± 57	57 ± 20	9.1 ± 3.4	21.3 ± 7.6
γjj	4.8 ± 7.4	52 ± 36	8 ± 11	20 ± 17
Zj, jj	0.06 ± 0.66	20 ± 14	5.9 ± 6.9	6.6 ± 7.8
$Z(\ell\bar{\ell})\gamma jj$	8.6 ± 2.5	6.8 ± 2.0	2.04 ± 0.95	2.2 ± 1.3
Total	735 ± 30	863 ± 54	271 ± 25	357 ± 30
Data	737	849	268	356

Table 2: Parameters of interest (POI) for the current analysis [1], the previous ATLAS analysis [11] sensitive to the low E_{T}^{γ} region and a combined result.

POI	Current analysis	Previous analysis	Combination
$\mu_{Z\gamma\mathrm{EWK}}$	0.78 ± 0.33	1.04 ± 0.23	0.96 ± 0.18
$\mu_{Z\gamma\mathrm{QCD}}$	1.21 ± 0.37	1.02 ± 0.41	1.17 ± 0.27
$\mu_{W\gamma}$	1.02 ± 0.22	1.01 ± 0.20	1.01 ± 0.13

5. Results

The observed (expected) signal significance for the current analysis is 3.2σ (3.7σ), while the combination with the mentioned above $Z(\nu\bar{\nu})\gamma jj$ ATLAS analysis in a low E_{T}^{γ} phase space [11] gives 6.3σ (6.6σ).

The fiducial cross-section in the phase-space region defined in Table 3 is predicted with `MadGraph5_aMC@NLO` and `Pythia` at leading order (LO) with next-to-leading order (NLO) QCD corrections and scale uncertainties computed with `VBFNLO`. It is $\sigma^{\mathrm{pred}}_{Z\gamma\mathrm{EWK}} = 0.98 \pm 0.02(\mathrm{stat.}) \pm 0.09(\mathrm{scale}) \pm 0.02(\mathrm{PDF})$ fb, while the observed one is $\sigma^{\mathrm{obs}}_{Z\gamma\mathrm{EWK}} = 0.77^{+0.34}_{-0.30}$ fb, and there is agreement between them. Here PDF is the parton distribution function.

The combined with $Z(\nu\bar{\nu})\gamma jj$ ATLAS analysis [11] result gives $\sigma^{\mathrm{pred}}_{Z\gamma\mathrm{EWK}}(\mathrm{comb}) = 9.6 \pm 1.0$ fb and $\sigma^{\mathrm{obs}}_{Z\gamma\mathrm{EWK}}(\mathrm{comb}) = 9.2 \pm 2.0$ fb in enlarged fiducial phase-space region without photon isolation and γ-centrality requirements and with $E_{\mathrm{T}}^{\gamma} > 15$ GeV.

Table 3: Fiducial phase-space region [1].

Selections	Value
$E_{\mathrm{T}}^{\mathrm{miss}}$	> 120 GeV
E_{T}^{γ}	> 150 GeV
Number of isolated photons	$N_{\gamma} = 1$
Photon isolation	$E_{\mathrm{T}}^{\mathrm{cone40}} < 0.022 p_{\mathrm{T}} + 2.45$ GeV, $p_{\mathrm{T}}^{\mathrm{cone20}}/p_{\mathrm{T}} < 0.05$
Number of jets	$N_{\mathrm{jets}} \geq 2$ with $p_{\mathrm{T}} > 50$ GeV
Overlap removal	$\Delta R(\gamma, \mathrm{jet}) > 0.3$
Lepton veto	$N_e = 0$, $N_{\mu} = 0$
$\lvert\Delta\phi(\gamma, \vec{p}_{\mathrm{T}}^{\,\mathrm{miss}})\rvert$	> 0.4
$\lvert\Delta\phi(j_1, \vec{p}_{\mathrm{T}}^{\,\mathrm{miss}})\rvert$	> 0.3
$\lvert\Delta\phi(j_2, \vec{p}_{\mathrm{T}}^{\,\mathrm{miss}})\rvert$	> 0.3
m_{jj}	> 300 GeV
γ-centrality	< 0.6

6. Systematic uncertainties

Table 4 shows the systematic uncertainties and their impact on the measured cross-section. The largest impact comes from the theoretical uncertainties of the $Z(\nu\nu)\gamma jj$ processes (both EWK and QCD).

Table 4: The systematic uncertainties and their impact on the measured cross-section [1].

Source of uncertainty	$\Delta\sigma/\sigma$ [%]
Experimental	
Jets	−3.2 / +3.4
Electrons and photons	−0.3 / +1.7
Muons	−0.4 / +0.5
E_{T}^{miss}	−1.8 / +2.2
Pile-up modelling	−1.7 / +3.2
Trigger efficiency	−0.9 / +2.1
Luminosity	−1.2 / +2.6
Theory	
$Z(\nu\bar{\nu})\gamma jj$ EWK/QCD interference	−0.6 / +2.6
$Z(\nu\bar{\nu})\gamma jj$ EWK process	−6 / +12
$Z(\nu\bar{\nu})\gamma jj$ QCD process	−15 / +16
Other processes	−5.3 / +7.7
Other sources	
Data-driven backgrounds	−0.9 / +1.2
Pile-up background	−1.2 / +2.6
$Z(\nu\bar{\nu})\gamma jj$ QCD m_{jj} modelling	−4.4 / +4.4

7. Effective Field Theory

Search for new physics in VBS processes is based on a general model-independent approach – Effective Field Theory (EFT) [12]. It parametrises the possible BSM physics contributions in the following Lagrangian $\mathcal{L}$ with the SM part (the first term) and the BSM part (other two terms) with dimension-6 and dimension-8 operators O:

$$\mathcal{L} = \mathcal{L}^{\mathrm{SM}} + \sum_i \frac{c_i}{\Lambda^2} O_i + \sum_j \frac{f_j}{\Lambda^4} O_j,$$

where c_i and f_j are the numerical coefficients describing the underlying BSM physics, and Λ is the BSM physics energy scale.

For dimension-6, there are QGCs and trilinear GCs (TGCs), while dimension-8 contains aQGCs and no aTGCs. Diboson production [13] results in high sensitivity to aTGCs. Thus, only dimension-8 operators are considered in the analysis. All the QGC vertices altered with dimension-8 operators are presented in Table 5. Here operators are classified as **M**ixed and **T**ransverse according to the number of gauge-boson strength fields contained in the operator (2 and 4, respectively) [14].

The following Wilson coefficients for dimension-8 operators are considered in the analysis: f_{M0}/Λ^4, f_{M1}/Λ^4, f_{M2}/Λ^4 (f_{MX} couplings), and f_{T0}/Λ^4, f_{T5}/Λ^4, f_{T8}/Λ^4, f_{T9}/Λ^4 (f_{TX} couplings).

Table 5: QGC vertices induced by dimension-8 operators. The blue row corresponds to the vertex allowed in the SM. The orange rows show the aQGCs.

	O_{M0}, O_{M1}, O_{M7}	$O_{M2}, O_{M3}, O_{M4}, O_{M5}$	O_{T0}, O_{T1}, O_{T2}	O_{T5}, O_{T6}, O_{T7}	O_{T8}, O_{T9}
$WWWW$	X		X		
$WWZZ$	X	X	X	X	
$ZZZZ$	X	X	X	X	X
$WWZ\gamma$	X	X	X	X	
$WW\gamma\gamma$	X	X	X	X	
$ZZZ\gamma$	X	X	X	X	X
$ZZ\gamma\gamma$	X	X	X	X	X
$Z\gamma\gamma\gamma$			X	X	X
$\gamma\gamma\gamma\gamma$			X	X	X

It should be noticed that f_{T8} and f_{T9} couplings can be probed only by the neutral quartic vertices (Table 5).

Figure 5 illustrates higher sensitivity to the aQGCs at high E_{T}^{γ} values (as it is mentioned in Section 2) for the f_{T0} and f_{M0} couplings.

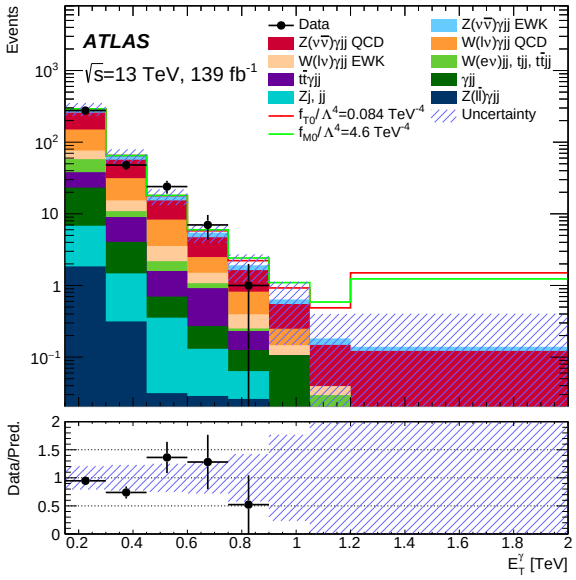

Figure 5: E_{T}^{γ} distribution in the SR with the number of events in the case of non-zero EFT coefficient f_{T0}/Λ^4 (f_{M0}/Λ^4) with the value shown in the legend [1].

8. Evolution of the expected and observed limits

Non-unitarised limits correspond to the case when the amplitudes predicted by the EFT can violate the unitarity by breaking the gauge structure of the model. These limits allow the different

channels and experiments to be compared, but the results are not physical. Unitarised limits, which are calculated by cutting the EFT terms above the unitarity limit, cannot be used for such a comparison, their calculation is more complicated, but they are more physical limits. To preserve unitarity at high energies, a clipping technique is used: the anomalous signal contribution is set to zero for $m_{Z\gamma} > E_c$, where E_c is a cut-off scale, based on the unitarity bounds for a given limit value calculated from partial-wave unitarity constraints [15].

Evolution of the expected (observed) limits as a function of the E_c for the f_{TX} and f_{MX} couplings are shown in Figures 6 and 7, respectively. Intersection point of the limit with the unitary bound corresponds to the E_c for unitarised limits.

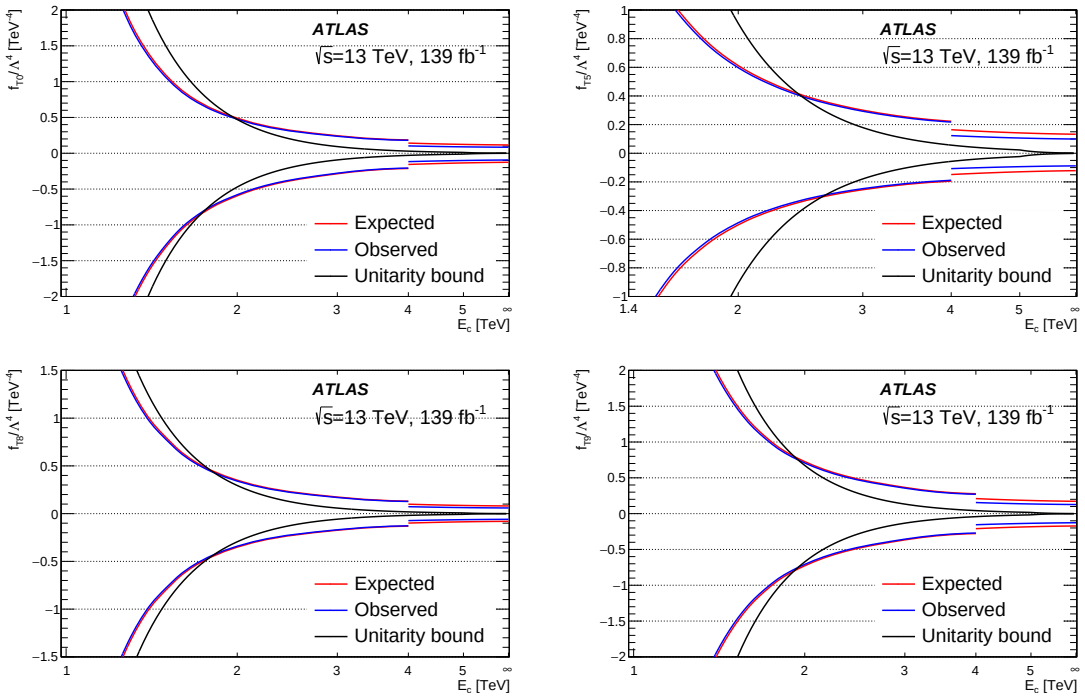

Figure 6: The expected (red) and observed (blue) limits as a function of the E_c for the f_{TX} couplings with the unitarity bound (black) [1].

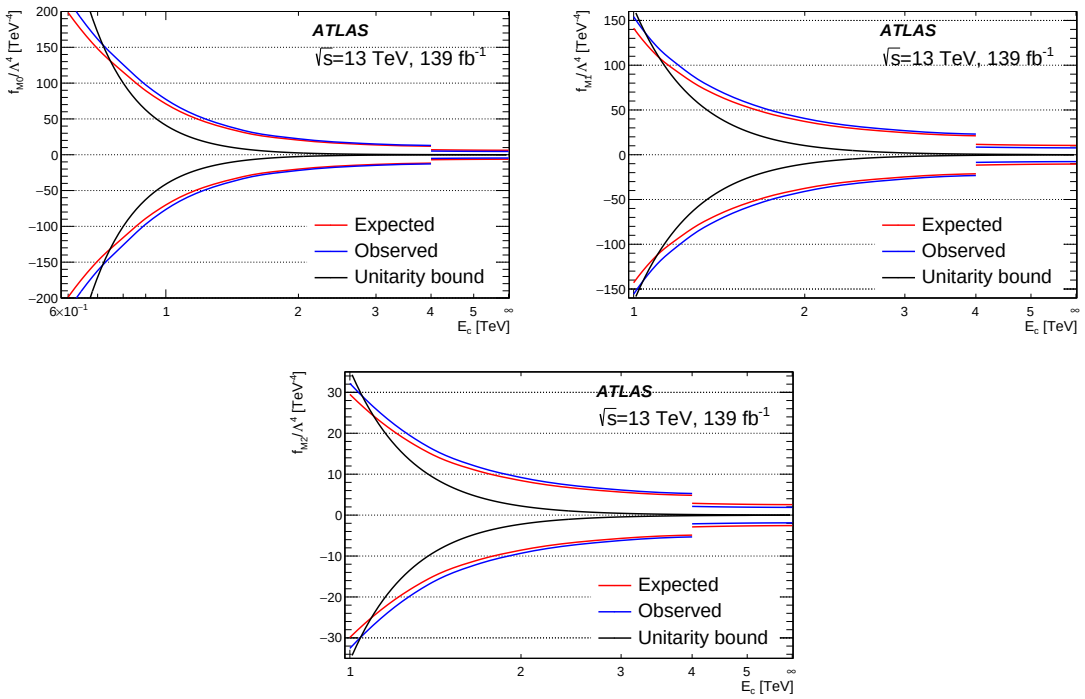

Figure 7: The expected (red) and observed (blue) limits as a function of the E_c for the f_{MX} couplings with the unitarity bound (black) [1].

9. Limits on aQGCs

Tables 6 and 7 contain observed and expected limits on the Wilson coefficients in non-unitarised and unitarised cases, respectively. A comparison of the latest results on the Wilson coefficients limits for the different analyses is shown in Table 8. The constraints on f_{T5}/Λ^4, f_{T8}/Λ^4, f_{T9}/Λ^4 coefficients are significantly stringent than those previously published for $Z(\ell\bar{\ell})\gamma jj$ [16], $ZZjj$ [17], and $W\gamma jj$ [18] analyses by the CMS collaboration [19]. The constraints on f_{T0}/Λ^4 and f_{M2}/Λ^4 coefficients are more stringent than those previously published for $WW/WZ/ZZ + jj$ CMS analyses [20].

Table 6: Observed and expected limits on the Wilson coefficients in non-unitarised case [1].

Wilson coefficient	Observed limit [TeV^{-4}]	Expected limit [TeV^{-4}]
f_{T0}/Λ^4	$[-9.4, 8.4] \times 10^{-2}$	$[-1.3, 1.2] \times 10^{-1}$
f_{T5}/Λ^4	$[-8.8, 9.9] \times 10^{-2}$	$[-1.2, 1.3] \times 10^{-1}$
f_{T8}/Λ^4	$[-5.9, 5.9] \times 10^{-2}$	$[-8.1, 8.0] \times 10^{-2}$
f_{T9}/Λ^4	$[-1.3, 1.3] \times 10^{-1}$	$[-1.7, 1.7] \times 10^{-1}$
f_{M0}/Λ^4	$[-4.6, 4.6]$	$[-6.2, 6.2]$
f_{M1}/Λ^4	$[-7.7, 7.7]$	$[-1.0, 1.0] \times 10^{1}$
f_{M2}/Λ^4	$[-1.9, 1.9]$	$[-2.6, 2.6]$

Table 7: Observed and expected limits on the Wilson coefficients in unitarised case [1].

Wilson coefficient	E_c [TeV]	Observed limit [TeV^{-4}]	Expected limit [TeV^{-4}]
f_{T0}/Λ^4	1.7	$[-8.7, 7.1] \times 10^{-1}$	$[-8.9, 7.3] \times 10^{-1}$
f_{T5}/Λ^4	2.4	$[-3.4, 4.2] \times 10^{-1}$	$[-3.5, 4.3] \times 10^{-1}$
f_{T8}/Λ^4	1.7	$[-5.2, 5.2] \times 10^{-1}$	$[-5.3, 5.3] \times 10^{-1}$
f_{T9}/Λ^4	1.9	$[-7.9, 7.9] \times 10^{-1}$	$[-8.1, 8.1] \times 10^{-1}$
f_{M0}/Λ^4	0.7	$[-1.6, 1.6] \times 10^{2}$	$[-1.5, 1.5] \times 10^{2}$
f_{M1}/Λ^4	1.0	$[-1.6, 1.5] \times 10^{2}$	$[-1.4, 1.4] \times 10^{2}$
f_{M2}/Λ^4	1.0	$[-3.3, 3.2] \times 10^{1}$	$[-3.0, 3.0] \times 10^{1}$

Table 8: Comparison of the limits on the Wilson coefficients for the different analyses. All coupling parameter limits are in TeV^{-4}. Bold indicates the most stringent constraint.

Wilson coefficient	Current analysis [1]	$Z(\ell\bar{\ell})\gamma jj$ CMS [16]	$ZZjj$ CMS [17]	$W\gamma jj$ CMS [18]	$WW/WZ/ZZ + jj$ CMS [20]
f_{T0}/Λ^4	**$[-9.4, 8.4] \times 10^{-2}$**	[-0.64, 0.57]	[-0.24, 0.22]	[-0.6, 0.6]	[-0.12, 0.11]
f_{T5}/Λ^4	**$[-8.8, 9.9] \times 10^{-2}$**	[-0.58, 0.64]	–	[-0.5, 0.5]	–
f_{T8}/Λ^4	**$[-5.9, 5.9] \times 10^{-2}$**	[-0.47, 0.47]	[-0.43, 0.43]	–	–
f_{T9}/Λ^4	**$[-1.3, 1.3] \times 10^{-1}$**	[-0.91, 0.91]	[-0.92, 0.92]	–	–
f_{M0}/Λ^4	[-4.6, 4.6]	[-15.8, 16.0]	–	[-8.1, 8.0]	**[-0.69, 0.70]**
f_{M1}/Λ^4	[-7.7, 7.7]	[-35.0, 34.7]	–	[-12, 12]	**[-2.0, 2.1]**
f_{M2}/Λ^4	**[-1.9, 1.9]**	[-6.55, 6.49]	–	[-2.8, 2.8]	–

10. Conclusion

$Z(\nu\bar{\nu})\gamma jj$ EWK production in the region of $E_T^\gamma > 150$ GeV using data collected by the ATLAS experiment during 2015-2018 from pp collisions at $\sqrt{s} = 13$ TeV and corresponding to an integrated luminosity of 139 fb^{-1} is presented.

The resulting observed (expected) signal significance is 3.2σ (3.7σ) which corresponds to evidence for this process in a boosted photon regime. The observed (expected) signal significance of the combination with the previously published ATLAS result with $15 < E_T^\gamma < 110$ GeV is 6.3σ (6.6σ).

The measured fiducial cross-section is $\sigma_{Z\gamma\text{EWK}} = 0.77^{+0.34}_{-0.30}$ fb which is in agreement with the SM prediction within the uncertainty.

Limits on aQGCs set on EFT dimension-8 operators are either competitive with or more stringent than previously published results.

References

[1] ATLAS collaboration, *Measurement of electroweak $Z(\nu\bar{\nu})\gamma jj$ production and limits on anomalous quartic gauge couplings in pp collisions at $\sqrt{s} = 13$ TeV with the ATLAS detector*, 2208.12741.

[2] ATLAS Collaboration, *The ATLAS Experiment at the CERN Large Hadron Collider*, *JINST* **3** (2008) S08003.

[3] ATLAS collaboration, *Object-based missing transverse momentum significance in the ATLAS detector*, *ATLAS-CONF-2018-038* (2018) https://cds.cern.ch/record/2630948.

[4] ATLAS Collaboration, *Performance of missing transverse momentum reconstruction with the ATLAS detector using proton–proton collisions at $\sqrt{s} = 13$ TeV*, *Eur. Phys. J. C* **78** (2018) 903 [1802.08168].

[5] ATLAS collaboration, *A new tool for measuring detector performance in ATLAS*, *J. Phys.: Conf. Ser.* **219** (2010) 032023. 9 p.

[6] ATLAS Collaboration, *Measurement of the inclusive isolated prompt photon cross section in pp collisions at $\sqrt{s} = 7$ TeV with the ATLAS detector*, *Phys. Rev. D* **83** (2011) 052005 [1012.4389].

[7] K. Cranmer, G. Lewis, L. Moneta, A. Shibata and W. Verkerke, *HistFactory: A tool for creating statistical models for use with RooFit and RooStats*, Tech. Rep. , New York U., New York (2012).

[8] J.H. Friedman, *Greedy function approximation: a gradient boosting machine*, *Annals of statistics* (2001) 1189.

[9] A. Hoecker et al., *TMVA - Toolkit for Multivariate Data Analysis*, physics/0703039.

[10] G. Cowan, K. Cranmer, E. Gross and O. Vitells, *Asymptotic formulae for likelihood-based tests of new physics*, *Eur. Phys. J. C* **71** (2011) 1554 [1007.1727].

[11] ATLAS Collaboration, *Observation of electroweak production of two jets in association with an isolated photon and missing transverse momentum, and search for a Higgs boson decaying into invisible particles at $\sqrt{s} = 13$ TeV with the ATLAS detector*, *Eur. Phys. J. C* **82** (2021) 105 [2109.00925].

[12] C. Degrande, N. Greiner, W. Kilian, O. Mattelaer, H. Mebane, T. Stelzer et al., *Effective field theory: A modern approach to anomalous couplings*, *Annals Phys.* **335** (2013) 21 [1205.4231].

[13] ATLAS Collaboration, *Measurement of the $Z\gamma \to \nu\bar{\nu}\gamma$ production cross section in pp collisions at $\sqrt{s} = 13$ TeV with the ATLAS detector and limits on anomalous triple gauge-boson couplings*, *JHEP* **12** (2018) 010 [1810.04995].

[14] R. Covarelli, M. Pellen and M. Zaro, *Vector-Boson scattering at the LHC: Unraveling the electroweak sector*, *Int. J. Mod. Phys. A* **36** (2021) 2130009 [2102.10991].

[15] E.d.S. Almeida, O.J.P. Éboli and M.C. Gonzalez-Garcia, *Unitarity constraints on anomalous quartic couplings*, *Phys. Rev. D* **101** (2020) 113003 [2004.05174].

[16] CMS Collaboration, *Measurement of the electroweak production of $Z\gamma$ and two jets in proton-proton collisions at $\sqrt{s} = 13$ TeV and constraints on anomalous quartic gauge couplings*, *Phys. Rev. D* **104** (2021) 072001 [2106.11082].

[17] CMS Collaboration, *Evidence for electroweak production of four charged leptons and two jets in proton-proton collisions at $\sqrt{s} = 13$ TeV*, *Physics Letters B* **812** (2021) 135992 [2008.07013].

[18] CMS Collaboration, *Observation of electroweak production of $W\gamma$ with two jets in proton-proton collisions at $\sqrt{s} = 13$ TeV*, *Physics Letters B* **811** (2020) 135988 [2008.10521].

[19] CMS Collaboration, *The CMS Experiment at the CERN LHC*, *JINST* **3** (2008) S08004.

[20] CMS Collaboration, *Search for anomalous electroweak production of vector boson pairs in association with two jets in proton-proton collisions at 13 TeV*, *Physics Letters B* **798** (2019) 134985 [1905.07445].